

Lahore

# Synthesis of Two-Dimensional MoS<sub>2</sub>-Perovskite Heterostructures

a dissertation presented  
by  
Rehan Ahmad  
to  
The Department of Physics

in partial fulfillment of the requirements  
for the degree of  
Bachelors of Science  
in the subject of  
Physics

Lahore University of Management Sciences  
, Pakistan  
May 2024

©2014 – Rehan Ahmad  
all rights reserved.

Thesis advisor: Professor Ammar Ahmed Khan

Rehan Ahmad

## Synthesis of Two-Dimensional MoS<sub>2</sub>-Perovskite Heterostructures

### ABSTRACT

Our research delves into the fields of two-dimensional (2D) materials, focusing on the creation of heterojunctions with potential applications in valleytronics. The study primarily centers on the integration of MoS<sub>2</sub> (Molybdenum Disulfide) and MBI (Metal Bismuth Iodide) perovskite on silicon aiming to exploit their unique properties for advanced electronic devices. A theoretical examination of interlayer excitons in two-dimensional system as well as the phenomenon of indirect-to-direct bandgap transition in MoS<sub>2</sub> will help justify our choice of material. Furthermore, we elaborate upon the Raman spectroscopic techniques and photoluminescence studies carried out in the laboratory for the realization of our structure. Building on the existing body of research on perovskite-TMDC junctions, we are poised to propose a novel junction type that promises fewer defects and enhanced performance in optoelectronic devices.

# Contents

o INTRODUCTION	<b>1</b>
0.1 What are Heterostructures? . . . . .	2
0.2 Staggered Heterostructures . . . . .	4
I THEORETICAL CONSIDERATIONS	<b>6</b>
1.1 Understanding Excitons . . . . .	6
1.2 Wannier-Mott Exciton Formalism . . . . .	8
1.3 Valleytronics . . . . .	12
1.4 Transition-metal dichalcogenide . . . . .	16
1.5 Molybdenum Disulfide . . . . .	18
1.6 Methylammonium Bismuth Iodide . . . . .	20
1.7 MoS <sub>2</sub> /MBI Heterostructure . . . . .	21
2 SPECTROSCOPIC EXPERIMENTS	<b>22</b>
2.1 Measuring phonon dispersion using Raman Spectroscopy . . . . .	25
2.2 Raman Spectroscopy Experiment . . . . .	28
2.3 Performing Raman on MoS <sub>2</sub> . . . . .	30
2.4 Photoluminescence studies . . . . .	34
2.5 Distinction between photoluminescence studies and Raman Scattering . . . . .	35
2.6 Exploring the PL process closely . . . . .	36
2.7 Equipment and Setup . . . . .	37
2.8 Photoluminescence Characteristics of MoS <sub>2</sub> . . . . .	38
2.9 Photoluminescence Spectroscopy of MoS <sub>2</sub> . . . . .	38
2.10 Temperature dependent Photoluminescence Spectroscopy of MBI .	40
3 SYNTHESIS IN LAB	<b>44</b>
3.1 Cleaning Silicon Wafer . . . . .	45
3.2 Dry Transfer of 2D Materials using PDMS layer . . . . .	46
3.3 Mechanical Exfoliation . . . . .	48

3.4	Looking for a monolayer under a microscope . . . . .	50
3.5	Synthesis of Heterojunction . . . . .	51
4	CONCLUSION	55
	REFERENCES	59

## Listing of figures

2.2	Phonon dispersion relation for a crystal with $N$ atoms per unit cell, showing optical and acoustic modes. Optical mode frequencies are $\omega_+ = \sqrt{\frac{2(K_1+K_2)}{m}}$ and $\omega_1 = \sqrt{\frac{K_2}{m}}$ , while the acoustic mode frequency is $\omega_- = \sqrt{\frac{K_1}{m}}$ . . . . .	25
2.3	Parabolic dispersion curve graph depicting why only some modes are accessed via Raman spectroscopy . . . . .	28
2.4	Our confocal geometry-based Raman spectroscopy lab setup . . . . .	29
2.5	2 points on the 2-Dimensional plane along the axis of a material . . . . .	32
2.6	Illustration of the Raman Active Modes in the 2H polytype . . . . .	33
2.7	Bulk to Monolayer transition. The two vertical lines show the frequencies of the $E_{12}^g$ and $A_1^g$ modes for 1L. . . . .	33
2.8	Schematic Representation of Photoluminescence Process. An electron in the valence band (left) is excited to the conduction band upon absorbing a photon (middle). The electron subsequently relaxes back to the valence band, emitting a photon in the process (right). The energy difference ( $\Delta E$ ) between the valence band (HOMO) and the conduction band (LUMO) determines the photon's energy. . . . .	35
2.9	The PL spectra of A and B Excitons for MoS <sub>2</sub> monolayer and bilayer	39
2.10	Temperature Dependent MBI in the temperature range of 88.4-295 K. . . . .	41
2.11	Deconvolved MBI PL Spectra. Intensity offset plotted for the temperature-dependent PL spectra of MBI. . . . .	43
3.1	Mechanical Exfoliation. Thinner layers are obtained by progressively pressing the tape to itself and unpeeling it. . . . .	48
3.2	MoS <sub>2</sub> flakes at x10 and x50 respectively. Often, monolayer and bilayers are found attached at the edge of bulk material . . . . .	50
3.3	MBI deposits on silicon at a magnification of 50x. (a) Mechanical exfoliation of MBI. (b) Deposits via direct contact between silicon and MBI. (c) Deposits by the PDMS transfer method . . . . .	52
3.4	Optical Images at 50x magnification. Figure on the left: MBI deposits on MoS <sub>2</sub> crystals on PDMS. Figure on the right: MoS <sub>2</sub> deposit on Si spin coated with MBI. . . . .	54

DEDICATED TO MY COLLEAGUES AND DEAREST FRIENDS IN THE PHYSICS DEPARTMENT...

# Acknowledgments

I WOULD LIKE TO EXPRESS my deepest gratitude to my thesis advisor, Dr. Ammar Ahmed Khan. His invaluable guidance and insightful feedback have been instrumental in the completion of my thesis. Throughout my initiation into the field, I have found him to be incredibly helpful. Whether it was my queries pertaining to the underlying theory or the challenges I faced in the lab, he was always ready to assist me in any possible way. Thank you very much for your support throughout this phase.

# 0

## Introduction

In his famous lecture “There’s Plenty of Room at the Bottom” addressed to the American Physical Society at Caltech on December 29, 1959, Richard Feynman explored the possibilities of manipulating matter at incredibly small scales. He foresaw the potential of miniaturization and nanotechnology in revolutionizing the landscape of material sciences, both of which serve as the backbone for the study of two-dimensional materials. In contrast to their three-dimensional counterpart, two-dimensional materials exhibit several interesting properties.

Their reduced length in the vertical direction facilitates downscaling and potentially make them a material-of-choice for electronics and optoelectronic devices<sup>15</sup>. More importantly for our aims, the Coulomb interaction between electrons and holes in 2-D materials is significantly higher. The heightened Coulomb interaction results in an extended exciton lifetime, potentially paving the way for the development of more energy-efficient solar cells.

Despite these benefits, 2D materials face several challenges in their implementation for practical purposes. Their low-carrier mobility and absorption rate severely limits their energy efficiency and restricts their applicability as photodetectors and biosensors. This leads us to explore the stacking of these 2D materials with other favorable materials to create a heterostructure. Towards these aims, we investigate the layering of two-dimensional Transition-Metal dichalcogenides (TMDCs) with a selected perovskite of our choice. Specifically, we investigate the interface between Molybdenum Disulfide (TMDC) and Methylammonium Bismuth Iodide. The following report details our attempts towards the creation of this structure, elaborating upon the underlying theory involving literature review, the spectroscopic studies to extract relevant data, and the experimental procedures such as mechanical exfoliation that have been carried out so far.

#### 0.1 WHAT ARE HETEROSTRUCTURES?

Standard commercial p-n solar cells are examples of homojunctions. In these structures, both the p and n junctions are made from the same semiconductor, typically crystalline silicon with a bandgap of 1.12 eV. The key difference lies in doping: one junction is n-doped while the other is p-doped. However, the bandgap of both the interfaces remains the same. On the other hand, in heterostructures the p and the n junctions are made from two or more different semiconductor materials. These materials typically have differing bandgaps and electronic

properties, leading to unique electronic and optoelectronic behavior not present in homojunctions.

The distinguishing characteristics of heterostructures are the band offsets. As a result of these, the band bending is more pronounced in heterostructures when the fermi level of both the p and n junction align. This leads to a more pronounced potential difference between p and n junction. As a consequence, the charge separation in heterostructures is more robust which reduces recombination effects.

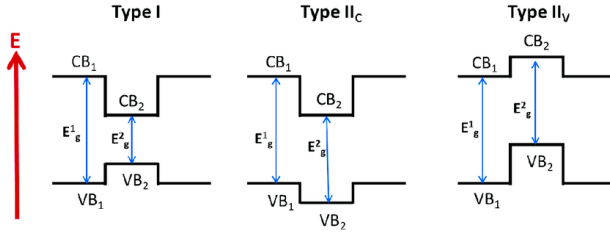


Figure 1: Type I and type II Quantum Well heterostructures. For the type I we have quantum wells for the carriers in both bands. For the type II heterostructures we have, in the same spatial region, a quantum well in one band, and, an energy barrier in the other band.

Depending on the band-offsets, heterostructures can be classified into three types:

1. **Type-I (Straddling Gap):** Both the conduction band minimum and the valence band maximum of one material lie within the bandgap of the other material. This configuration confines both electrons and holes in the same region.
2. **Type-II (Staggered Gap):** The conduction band minimum of one material and the valence band maximum of the other material lies at different sides of the heterojunction. This separates electrons and holes across the junction.
3. **Type-III (Broken Gap):** The conduction band minimum of one material is lower than the valence band maximum of the other material. This leads to a band alignment

that facilitates tunneling phenomena.

## 0.2 STAGGERED HETEROSTRUCTURES

Since our material of interest form staggered heterostructures, we explain some of the distinguishing properties of these junctions. This type of structure confines electrons in one material while holes in the other. As a result, the wavefunctions of electrons and holes overlap less compared to Type-I heterostructures. This means that the recombination of electrons and holes is typically slower, leading to increased carrier lifetimes. Furthermore, this spatial overlap directly aids in the formation of indirect excitons where the electrons and hole are bound across the interface. Considering the specificities of our heterostructure, The valence and conduction band of TMDC are lower than the valence and the conduction band of MBI respectively (see figure below). The range of spacing between the conduction band of MoS<sub>2</sub> and MBI are 0.46 eV and 0.81 respectively while the range of spacings between the valence band of MoS<sub>2</sub> and MBI are 0.15 eV and 0.23 eV respectively. As a result, holes are transported from the valence band of the TMDC to that of the perovskite and electrons from the conduction band of the perovskite are transported to that of TMDC. This creates the inter-layer excitons with the electron transfer being blocked<sup>5 13</sup>.

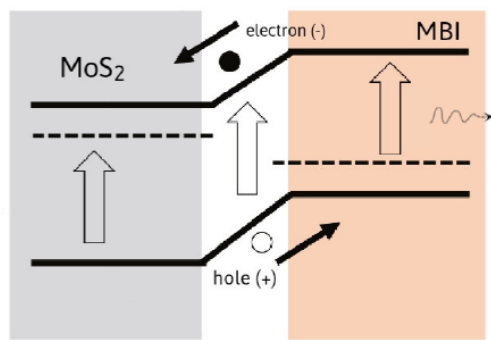


Figure 2: The Band Energy Diagram of MoS<sub>2</sub>-MBI Heterostructure. Displays the excitonic transfer mechanism between the conduction and valence bands of MBI and MoS<sub>2</sub>.

# 1

## Theoretical Considerations

### 1.1 UNDERSTANDING EXCITONS

In a direct bandgap transition, an electron absorbs a photon with energy  $\hbar\omega$  greater than the band gap  $E_g$ , thereby being excited from the valence band to the conduction band. In the process, it leaves behind a positively charged hole in the valence band. If we consider the absorption spectra of semiconductors, we expect the material to be transparent for energies less

than this threshold limit. However, experimentally, it is observed that there are sharp peaks of absorptions slightly below the band gap.<sup>7</sup> This is caused by the absorption of photon with the creation of bound electron-hole pairs. The negatively charged electron in the conduction band is bound to the positive hole, forming a quasi-particle called an exciton (X) with the following Coulomb potential<sup>9</sup>:

$$U(r) = \frac{e^2}{4\pi\epsilon_0\epsilon_r} \quad (1.1)$$

The exciton then is the bound state of electron-hole pair with Equation 1.1 being the exciton's binding energy. For standard semiconductors, the range of these binding energies is between 1 meV to 1 eV. Due to this binding energy, the energy required for excitations of electrons is lowered with respect to the threshold  $\hbar\omega > E_g$  (considering only direct transitions). It is to be noted that while excitons can move through the crystal and transport energy, they do not transport charge.

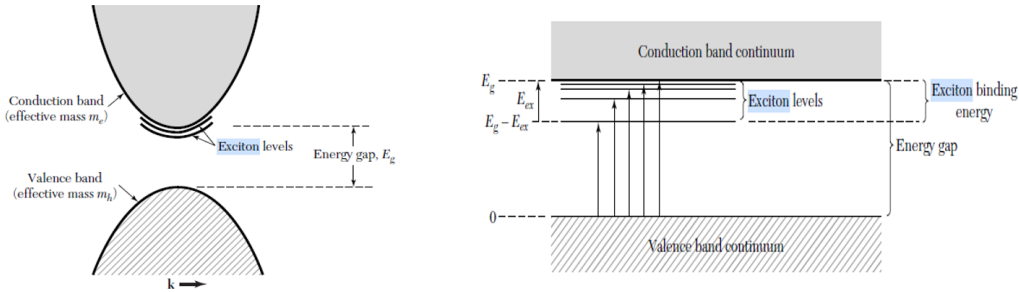


Figure 1.1: Figure on the Left: Exciton levels in relation to the conduction band edge, for a simple band structure with both conduction and valence band edges at  $k = 0$ . Figure on the right: Energy levels of an exciton created in a direct process. The binding energy of the exciton is  $E_{ex}$ , referred to a free electron and free hole.

A necessary condition for the formation of excitons is that the electron and hole group velocities are the same. This is because unlike single particle transitions in which a specific electron moves from a valence band to a conduction band with all other electrons remaining

in their respective states, excitonic transitions are collective excitations. In this scenario, the absorption of light does not merely excite a single electron; instead, it induces a collective response from many states within the electronic band structure. This collective nature is due to the strong Coulomb interaction between the excited electron and the hole left behind which leads to a correlated movement of these charge carriers.

There are two main types of excitons: Wannier-Mott Excitons (Free Excitons) and Frenkel Excitons (Bound excitons). Frenkel Excitons are mainly observed in insulators. They have a much smaller radius and a heavy effective mass. On the other hand, The Wannier-Mott excitons are mainly found in semiconductors. They have a sufficiently large radius that encompasses many atoms and therefore they can move freely throughout the crystal. This is because the relative permittivity in equation 1.1 for Wannier-Mott excitons is much greater than one unlike for Frenkel excitons, thereby screening the coulomb interaction. Furthermore, the effective mass of electron and holes in a crystal are typically smaller. Generally, organic matter such as fullerenes and insulators tend to exhibit Frenkel excitons while most inorganic or hybrid semiconductors such as perovskites have Wannier-Mott excitons.

## 1.2 WANNIER-MOTT EXCITON FORMALISM

Since excitons are bound-state of positively charged holes and negative charged-electron, they are hydrogenic system that can be modelled similarly to the bound state of a hydrogen atom. For Wannier-Mott Excitons, the mass of the electron is replaced with the effective mass of electron,  $m_e^*$ , and the relative permittivity  $\varepsilon_r$  of the material of interest is incorporated. In light of these considerations, equation 1.1 becomes our starting point.

We can then calculate the energies of the bound state in a similar manner as we do for the hydrogen atom. The effective Rydberg constant and effective Bohr radius with  $\varepsilon_0$  replaced by

$\varepsilon_0 \varepsilon_r$  and mass  $m$  replaced by effective mass  $m_e^*$ <sup>12</sup> are

$$R_y^{\text{eff}} = R_y \left( \frac{m_e^*}{m} \right) \frac{1}{\varepsilon_r^2} \quad (1.2)$$

$$\alpha_0^{\text{eff}} = \alpha_0 \left( \frac{\varepsilon_r m}{m_e^*} \right) \quad (1.3)$$

Where,

$$R_y = \frac{m_e^4}{8\varepsilon_0^2 b^2} \approx 13.6 \text{ eV} \quad (1.4)$$

$$\alpha_0 = \frac{4\pi\varepsilon_0 \hbar^2}{m_e^2} \approx 0.51 \times 10^{-10} \text{ m} \quad (1.5)$$

Consequently, the energy of Wannier-Mott excitons becomes the following:

$$E(n) = -\frac{R_y^{\text{eff}}}{n^2} = -\frac{R_y}{n^2} \left( \frac{m_e^*}{m} \frac{1}{\varepsilon_r^2} \right) \quad (1.6)$$

Furthermore, from equation 1.2, it follows that the radius of the excitons is the following:

$$r_n = \left( \frac{m \varepsilon_r \alpha_0}{m_e^*} \right) n^2 1.7 \quad (1.7)$$

### 1.2.1 EXCITONIC EFFECTS IN 2D

To understand how excitonic effects are more pronounced in 2D materials, we solve the Hydrogen problem in 2-dimension non-relativistically<sup>14</sup>. In polar coordinates, the Schrödinger

Equation becomes the following:

$$\left[ -\frac{\hbar^2}{2m_e} \left( \frac{\partial}{\partial r^2} + \frac{1}{r} \frac{\partial}{\partial r} + \frac{1}{r^2} \frac{\partial^2}{\partial \phi^2} \right) - \frac{Ze^2}{r} \right] \psi(r, \phi) = E\psi(r, \phi) \quad (1.8)$$

Using separation of variables,

$$\psi(r, \phi) = R(r)\Phi(\phi) \quad (1.9)$$

We obtain:

$$\Phi(\phi) = \frac{1}{(2\pi)^{1/2}} e^{il\phi}, \quad l = 0, \pm 1, \pm 2, \dots \quad (1.10)$$

$$\frac{d^2}{dr^2} R(r) + \frac{1}{r} \frac{d}{dr} R(r) + \left[ \frac{2m_e}{\hbar^2} \left( E + \frac{Ze^2}{r} \right) - \frac{l^2}{r^2} \right] R(r) = 0 \quad (1.11)$$

From equation 1.10, we see that the spherical symmetry of the classical 3D problem is preserved so that the angular momentum along the z-direction commutes with the Hamiltonian:

$$\hat{L}_z = i\hbar \frac{\partial}{\partial \phi} \quad (1.12)$$

Which commutes with the Hamiltonian. Hence,  $l$  is a good quantum number. On solving the radial equation for the Discrete Spectrum  $E < 0$ , we define (cite Landau and Lifshitz here):

$$E = -\frac{Z^2}{2N^2} \left( \frac{m_e e^4}{\hbar^2} \right) \quad (1.13)$$

$$r = \frac{N\hbar^2}{2m_e Ze^2} x = \frac{1}{\beta_N} x \quad (1.14)$$

$$R(x) = x^l e^{-x/2} G(x) \quad (1.15)$$

Subsequently, the radial equation in 1.11 becomes the following:

$$x \frac{d^2G}{dx^2} + [(2|l| + 1) - x] \frac{dG}{dx} - \left( -N + |l| + \frac{1}{2} \right) G = 0 \quad (1.16)$$

The solution to this is the confluent hypergeometric function<sup>8</sup>:

$$G(x) = F_1 \left( -N + |l| + \frac{1}{2}, 2|l| + 1, x \right) \quad (1.17)$$

A solution which satisfies the condition at infinity is obtained only for negative integral (or zero) values of  $-N + |l| + \frac{1}{2}$ , otherwise 1.17 diverges. Thus, we arrive at the condition:

$$N = \frac{1}{2}, \frac{3}{2}, \frac{5}{2}, \dots \quad (1.18)$$

Let

$$n = N + \frac{1}{2} = 1, 2, 3, \dots \quad (1.19)$$

Where  $n$  is the principal quantum number. For a given  $n$ ,  $|l|$  can take the values:

$$|l| = 0, 1, 2, \dots, n - 1 \quad (1.20)$$

Rescaling, we obtain the 2D energy eigenvalues:

$$E_n = -\frac{Z^2}{2(n - \frac{1}{2})^2} \left( \frac{m_e e^4}{\hbar^2} \right) \quad (1.21)$$

Thus, the energy levels in 2D excitons can be estimated as thus,

$$E_n = -\frac{1}{2(n - \frac{1}{2})^2} \left( \frac{m_e^* e^4}{\hbar^2} \right) \quad (1.22)$$

For  $n = 1$ , we see from Equation 1.22 that the binding energy is four times larger for two-dimensional excitons than three-dimensional excitons, highlighting how they are more stable in lower-dimensional systems. As stated in our preliminary discussion, this is one of the central appeals for considering two-dimensional materials over their three-dimensional counterparts.

It is to be noted that the hydrogen model is not effective for lower energy states in inhomogeneous dielectric environments. Chernikov et al. demonstrated this with WS<sub>2</sub> monolayers<sup>2</sup>. However, the model performs better for higher energy excited states because the wave function of a tightly bound exciton extends outside the monolayer, where reduced screening results in a stronger binding energy (EB). Alternative models are used to account for this deviation in transition metal dichalcogenides (TMDCs)<sup>11,6</sup>

### 1.3 VALLEYTRONICS

One of the many appeals of two-dimensional materials is their central role in the emerging field of Valleytronics. This involves the utilization of the valley degree of freedom of charge carriers for information processing. For many two-dimensional materials with hexagonal lattice structures such as graphene or transition metal dichalcogenides (TMDs), the formation of excitons is influenced by the electronic band structure including the  $\mathbf{k}$  and  $\mathbf{k}'$  valleys.

To explain the concept of valleys and their properties, let us consider the graphene monolayer which holds an important place in the study of material sciences. Since graphene has a hexagonal crystal lattice structure, our subsequent discussion readily holds for TMDCs. When we diagonalize the Hamiltonian associated with graphene in  $\mathbf{k}$ -space, we obtain its band structure which tells us the set of quantum energy levels associated with it. However, in the case of graphene, the band structure ends up looking quite complicated. Therefore to

simplify our analysis, we leverage the fact that graphene is charge neutral. The charge neutrality of graphene implies that its electronic energy states are usually filled up with electrons to a very specific point called the charge neutrality point about which we can expand and forget about higher and lower energies. Doing this results in a simplification of the material band structure to a simpler picture which involves six linearly dispersing cones, usually referred to as Dirac Cones since they represent the energy-momentum relationship of the Dirac Particles in Quantum Field Theory.

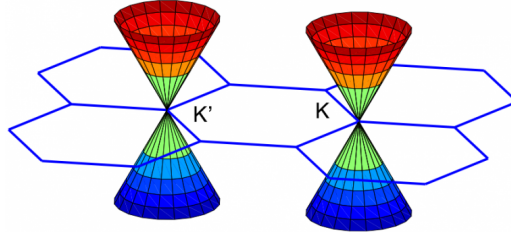


Figure 1.2: 2D hexagonal Brillouin zone and band edge (K points) structure of MoS2

For graphene, three of these six-linearly dispersed cones end up being entirely equivalent to each other. As such we focus on the two independent cones located at the point of momentum space  $\vec{k}$  and  $\vec{k}'$  (see figure)

These independent set of cones are known as the K and K' valleys being centered around the K and K' points in reciprocal space. The properties they result in are closely related to a spin-like property of the electrons in the graphene known as pseudospin. The K valley is considered to be "pseudospin up" and the K' valley is considered as "pseudospin down". An electron can also be in a superposition of pseudospin up and down. The resemblance with spin comes from the fact that scattering processes between the two valleys are fairly rare, and so pseudospin is conserved over some distance. Due to pseudospin, besides the normal degeneracy factor of 2 from actual spin, the electrons in graphene have a further factor of 2 degeneracy from the valleys spin. Note that pseudospin is not associated with a magnetic moment

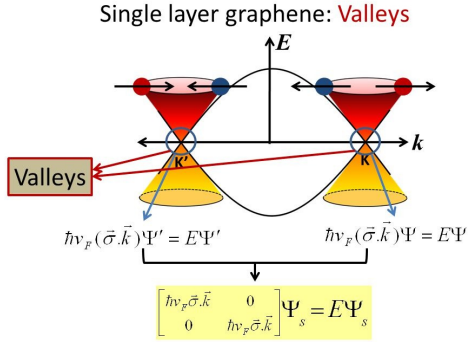


Figure 1.3: The figure displays the linear energy dispersion near the Dirac points ( $K$  and  $K'$ ) in single-layer graphene, highlighting the valleys. The equations describe the energy eigenvalues, illustrating the behavior of Dirac fermions in the graphene lattice.

unlike real spin.

In the  $k$  and  $k'$  valleys, the electrons and holes have nearly equal and opposite momenta, which allows for efficient exciton formation through the Coulomb interaction between electrons and holes. This momentum conservation is a crucial factor favoring exciton formation in these valleys. The energy minimum in the bandgap at the  $K$  and  $K'$  valleys means that the energy required to create an electron-hole pair (i.e., the exciton binding energy) is lower in these valleys compared to other points in the Brillouin zone. As such, lower binding energy makes exciton formation more stable and likely in these regions.

In hexagonal structure,  $k$  and  $k'$  are related to each other by spatial inversion of one another:

$$\vec{r}_k \rightarrow -\vec{r}'_k \quad (1.23)$$

Note that subjecting a system to spatial inversion doesn't necessarily mean that we are going to find spatial inversion symmetry. For our material of interest, Molybdenum disulfide ,

this spatial inversion symmetry does not hold as the operation of inverting a vector that connects two atoms does not yield a corresponding vector that connects two-atoms in the crystal structure.

Furthermore, any material obeys time-reversal symmetry unless this symmetry gets broken by an external magnetic field:

$$t \rightarrow -t \quad (1.24)$$

For Valleytronics, we somehow aim to differentiate electrons /holes/excitons that are located in each valley K and K' since these valleys are not equivalent. If we find a way to distinguish the valley information of electrons/hole/exciton, then we can ascribe a valley index  $\tau_z = \pm 1$  to the electrons/hole/exciton and carry out applications ascribed with spintronics. One of the important concepts related to valleys that we are interested is in the valley lifetime.

Valley lifetime is the property that tells us for how long valley information will be intact. For example, if we shine light of  $\sigma_+$  circular polarization on our sample and we accumulate particles in the  $K_1$  valley, the valley lifetime tells us for how long they're going to stay in that  $K_1$  valley before they scatter to the  $K_2$  valley. This valley lifetime is very important because all reliable valley processing and manipulation operations have to take place within that lifetime. Therefore ideally our valley lifetime would be as long as our particle lifetime.

Usually, valley lifetime of excitons is short. They vary between 0.1 to 100 picoseconds, depending on what transition metal you choose and what experimental setup you have. This valley life is much shorter than the actual Exciton lifetime, so the recombination lifetime is about 10 picoseconds. The dominant mechanism that causes this short valley lifetime of excitons is not yet entirely clear. One of the central appeals of the heterostructure that we are creating is that the lifetime of interlayer excitons is usually higher than the intralayer excitons,

thereby increasing their valley lifetime.

The unique properties of interlayer excitons arise from the spatial separation of the electron and hole between different layers. This spatial separation results in a weaker Coulomb interaction compared to intralayer excitons. As a result, interlayer excitons have longer lifetimes and can exhibit stronger binding energies than their intralayer counterparts. This makes them attractive for various optoelectronic applications, as their long lifetimes can lead to enhanced light emission and more efficient energy transfer processes.

Besides valley lifetime, valley manipulation and valley transport are ideas of interest to us. Valley manipulation is all about how we can manipulate particles depending on their values properties. We can do that with optical control, valley hall effect and valley magnetic control. One particular way of manipulating valley information is through the polarization of light. Right-handed circularly polarized light (RHCP) can excite excitons in the  $k$  valley while left-handed circularly polarized light (LHCP) can excite excitons in the  $k'$  valley.

#### 1.4 TRANSITION-METAL DICHALCOGENIDE

TMDCs are a class of materials that consist of transition metal atoms (e.g., molybdenum, tungsten) sandwiched between two layers of chalcogen atoms (e.g., sulfur, selenium). These materials are typically arranged in a hexagonal lattice structure.

The reason why TMDCs are so central to the semiconductor industry is because TMDCs and graphene are examples of two-dimensional materials and TMDCs can serve as a better alternative to graphene. For example, let us consider the electronic properties of the two.

Graphene is a semimetal with massless Dirac fermions, which means that it has zero bandgap, and its electrons behave as if they have no rest mass leading to high electron mobility. To address this, researchers have attempted to engineer a band gap in graphene by methods such as

laterally confining graphene nanoribbons, applying an electric field to bilayer graphene and interacting it with suitable substrates. However, these methods have been unsatisfactory because creating even a small band gap such as 0.4 eV in graphene nanoribbons significantly reduces electron mobility. TMDCs, in contrast, are semiconductors with a finite bandgap. This bandgap makes them more suitable for certain electronic and optoelectronic applications where the ability to control electron flow is crucial. Similarly, consider their optical properties. Graphene is nearly transparent and absorbs only a small fraction of light across a broad wavelength range. On the other hand, TMDCs have a higher light absorption ability due to their bandgap in the visible and near-infrared light range, making them useful for light-harvesting and photodetector applications. The reason for this increased absorption rate is due to electron occupation rate of the non-bonding d orbitals of the transition metal atoms with the number of electrons occupying a d orbital depending on the group of the chosen TMDC.

TMDCs can exist in three different phases: tetragonal (nT), hexagonal (nH), and rhombohedral (nR). The phase nomenclature (e.g., 1H) indicates the number of layers per unit cell and the crystal symmetry. MoS<sub>2</sub> monolayers typically exist in the 1H phase due to its thermodynamic stability which requires the least activation energy. Phase transitions can be induced by chemical or electrostatic doping, affecting the material's metallic or semiconducting nature and making them useful in contact resistance engineering.

The arrangement of transition metal atoms and the occupation of their d orbitals significantly impact the electronic structure of TMDCs. In 2H and 1T structures, non-bonding d bands are located within the gap defined by the bonding and antibonding M-X bands. In 2H TMDCs, the d orbitals split into three groups, influencing the material's semiconducting behavior. For example, the complete occupation of the lowest energy dz<sup>2</sup> orbital with non-bonding electrons in MoS<sub>2</sub> explains its semiconducting properties. In contrast, the 1T phase

exhibits metallic behavior due to its different orbital arrangements.

One of the most significant properties of TMDCs is their indirect-to-direct bandgap transition as we go from bulk to single monolayer. This direct bandgap of monolayer allows them to directly emit a photon since the crystal momentum of the material is conserved unlike in the case of the bulk where a phonon has to be emitted together with a photon in order for crystal momentum to be conserved (Simon, page 179).

## 1.5 MOLYBDENUM DISULFIDE

The choice of TMDC in our experiment was Molybdenum Disulfide for multiple reasons. The bandgap of Molybdenum Disulfide is around  $\sim 1.85$  eV which matches with the bandgap of the perovskite MBI used in the experiment. Secondly, Molybdenum Disulfide has been found to exhibit high carrier mobility which is the measure of how quickly charge carriers can move through a material under the influence of an electric field. High carrier mobility is beneficial for electronic devices as it facilitates the rapid movement of charge carriers. This reduces the chances of recombination and improves overall efficiency. Thirdly, the bandgap of Molybdenum Disulfide can be tuned by altering the number of layers or introducing strain. This tunability allows for optimization of its electronic properties for specific applications.

Finally, the indirect to direct bandgap transition of Molybdenum Disulfide allows the monolayer to absorb 10 percent incident light with energy above the band gap which is a thousand-fold increase in PL from the material in its bulk form<sup>10</sup>.

The indirect-to-direct bandgap transition can be seen in the figure below which has been calculated using density functional theory (DFT). DFT is used to investigate the electronic structure of many-body systems. For systems with many electrons, directly dealing with the wavefunction becomes computationally intractable. DFT simplifies this problem by focusing

on the electron density. The foundation of DFT lies in two theorems proposed by Hohenberg and Kohn. The first theorem states that the ground-state properties of a many-electron system are uniquely determined by its electron density. The second theorem asserts that there is a specific functional of the electron density that when minimized yields the exact ground-state energy and density of the system.

In the Kohn-Sham approach, a hypothetical system of non-interacting electrons that has the same ground-state electron density as the real interacting system is introduced. The idea is to solve a set of simpler equations for this non-interacting system and then use the solution obtained to approximate the properties of the real system.

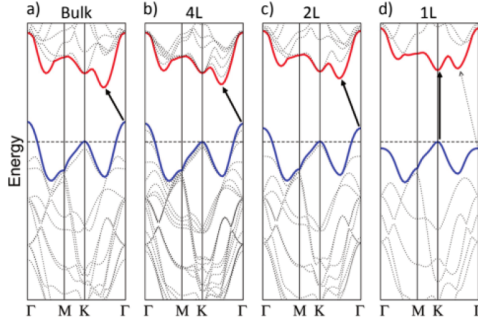


Figure 1.4: Energy band diagrams showing the widening of and change from an indirect to direct band gap as the number of layers decreases

We have already talked about  $\vec{k}$  and  $\vec{k}'$  valleys in context of 2D hexagonal structures. In the literature, the exciton produced in the  $k$  valley of Molybdenum Disulfide is called A exciton while that produced in the  $k'$  valley is called the B exciton. The ideas discussed under the subsection valleytronics are directly applicable to Molybdenum Disulfide, including but not limited to valley information, valley lifetime, and spin-valley coupling.

## 1.6 METHYLAMMONIUM BISMUTH IODIDE

The choice of perovskite in the experiment was methylammonium bismuth iodide (MBI) for multiple reasons. The bandgap of MBI's conduction band and valence band aligns with that of Molybdenum Disulfide. Moreover, choosing a perovskite with bismuth as its constituent supports our desire to move away from lead-based perovskites which decay to lead iodide at temperatures above 85 °C. Since lead iodide is a water-based carcinogen, our choice of MBI is an environmentally friendly alternative. Functionally, Bi has a high absorption coefficient which means light is able to penetrate deeper through it, which supports our aim of complementing it with MoS<sub>2</sub> capabilities as we will discuss in the next section. Finally, MBI is easily synthesizable in the lab and is the perovskite of our choice in the research group.

The figure below shows the structure of MBI under a scanning electron microscope under different resolutions, with flakes displaying a flower-like pattern of being approximately 5  $\mu\text{m}$  wide and 1  $\mu\text{m}$  thick.

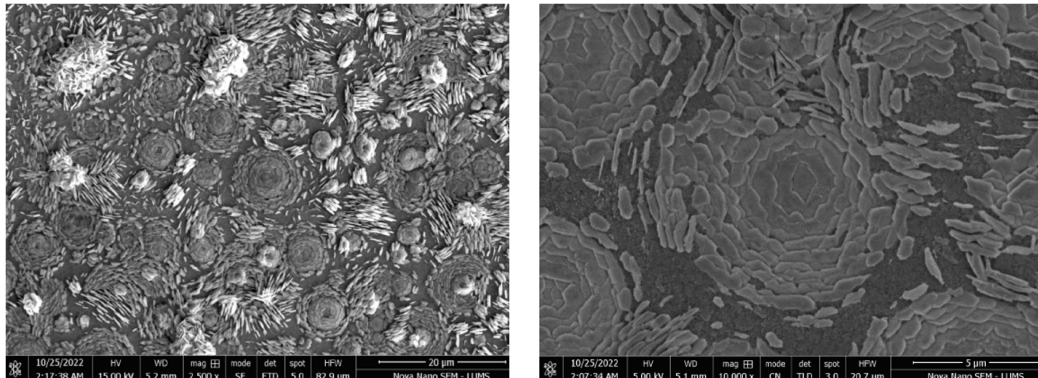


Figure 1.5: Scanning electron microscope (SEM) images of flower-like MBI deposits at set resolution. Figure on the left has a resolution of 5  $\mu\text{m}$  and figure on the right has a resolution of 20  $\mu\text{m}$ .

## 1.7 MoS<sub>2</sub>/MBI HETEROSTRUCTURE

Monolayer MoS<sub>2</sub> has a direct bandgap of 1.8 eV. It absorbs 5-10% of the incident light within the range of 510-780 nm, which is one order of magnitude higher than the absorption of Si<sup>1</sup>, which is the industrial material of choice when it comes to optoelectronic materials. This makes MoS<sub>2</sub> a viable option in a wide variety of applications such as optical modulators, photodetectors, and supercapacitors. However, despite this superior ability to absorb light in the 510-780 nm range, it is physically difficult for MoS<sub>2</sub> to absorb sufficient light because of its atomically thin thickness. This prevents the successful integration of MoS<sub>2</sub>-based optoelectronic devices. Perovskites, on the other hand, have large absorption efficiency and long carrier diffusion length. As a result, light can penetrate deeper into the material before being absorbed, and this generally increases the amount of absorption occurring throughout the material. This complementary combination can enhance the overall performance of optoelectronic devices by leveraging the superior light absorption of MoS<sub>2</sub> along with the large absorption coefficient of Perovskites.

# 2

## Spectroscopic Experiments

When light interacts with a sample, a portion of the incident light reflects off its surface, while the remaining light penetrates the sample. Within the sample, light may undergo absorption if its frequency resonates with the transition frequencies of the medium, or it may scatter if its direction (and potentially its frequency) changes upon interaction with the medium. The mechanisms for light scattering or absorption include Rayleigh scattering, Raman scattering, and PL absorption.

In the case where the light emerging from the sample retains the same frequency as the incident light ( $\omega_i$ ), Rayleigh scattering takes place.

- If the scattered light exhibits a different frequency than  $\omega_i$ , Raman scattering occurs.
- For the process of Photoluminescence (PL) absorption, absorbed light is immediately re-emitted without undergoing scattering.

Let us consider Rayleigh scattering and Raman scattering more closely.

- Rayleigh Scattering occurs when the scattered light has the same energy as the light that initially struck the sample. This means that the elastically scattered light will have the same frequency, wavelength, and color as the original beam of light.
- Raman Scattering occurs when the scattered light has a different energy than the light that initially struck the sample. This means the inelastically scattered light will have a different frequency, wavelength, and color than the original beam of light.

We can subdivide Raman scattering into two cases. The frequency of the scattered light may be larger (anti-Stokes scattering) or smaller (Stokes scattering) than that of the incident photons. The Figure depicts these types of scattering.

Raman scattering can be considered an inelastic collision of an incident photon  $\hbar\omega_i$  with a molecule in the initial energy level  $E_i$ . After the collision, a photon,  $\hbar\omega_f$ , with lower energy is detected, and the molecule is found in a higher energy level  $E_f$ <sup>3</sup>.

The energy difference:

$$\Delta E = E_f - E_i \quad (2.1)$$

is imparted to the molecule.

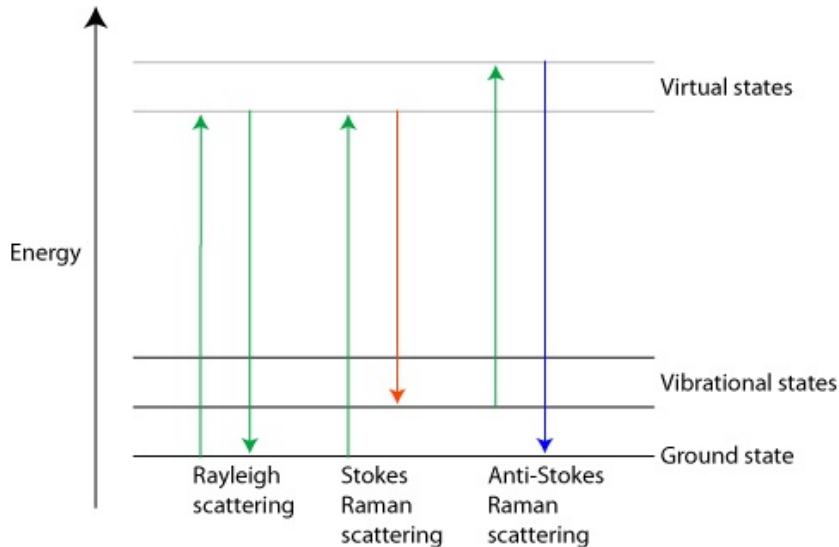


Figure 2.1: Energy diagram showing different types of scattering. The arrows indicate transitions between ground, vibrational and virtual states, highlighting the differences in energy changes associated with each type of scattering.

To understand the effect of the imparted energy  $\Delta E$  on the molecule during inelastic scattering, we must consider the electromagnetic nature of light. The interaction of light with the molecule causes the charges of the molecule to move in the direction opposite to the driving potential<sup>4</sup>. This shift in the electron cloud of the molecule polarizes it and in return causes the molecule to act as a dipole. It is to be noted that this oscillation of charges generates its own time-varying electric field which in turn generates electromagnetic radiation. This radiation is emitted in all directions, including the same direction as the incident light. However, the radiation emitted by the molecule is typically very weak and is not usually detected.

These molecular vibrations of the charges are quantized meaning they can only exist at specific energy levels. Therefore, when a photon from the incident light transfers energy to a molecule during Raman scattering, it can cause the molecule to change its vibrational energy level. This change in vibrational energy corresponds to the creation (or destruction) of what

are called phonons

## 2.1 MEASURING PHONON DISPERSION USING RAMAN SPECTROSCOPY

A crystal with  $N$  atoms per unit cell has  $3N$  vibrational modes and  $3N - 3$  optical modes

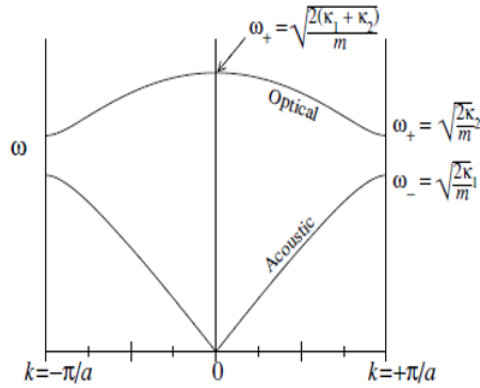


Figure 2.2: Phonon dispersion relation for a crystal with  $N$  atoms per unit cell, showing optical and acoustic modes. Optical mode frequencies are  $\omega_+ = \sqrt{\frac{2(K_1+K_2)}{m}}$  and  $\omega_1 = \sqrt{\frac{K_2}{m}}$ , while the acoustic mode frequency is  $\omega_- = \sqrt{\frac{K_1}{m}}$ .

We can measure the phonon dispersion relation ( $\omega$  with respect to  $k$ ) through light scattering. For a solid to interact with a particle, we must shine a beam of particle onto the lattice (see the figure above). This would cause the external particle to interact with the lattice. During this interaction, momentum and energy are exchanged between the external particle and the phonon. By carefully measuring the changes in momentum and energy of the external particle, we can effectively determine the momentum and energy of the phonon. This process adheres to conservation laws, expressed as following:

$$\vec{k}_{\text{in}} = \vec{k}'_{\text{out}} + \vec{q} \quad (2.2)$$

Where  $\vec{q}$  is the momentum of the phonon,  $\vec{k}_{\text{in}}$  is the momentum of the external particle before it interacts with the phonon, and  $\vec{k}'_{\text{out}}$  is the momentum after it interacts with the phonon.

The energy conservation is given by:

$$\varepsilon(\vec{k}_{\text{in}}) = \varepsilon(\vec{k}'_{\text{out}}) + \hbar\omega(\vec{q}) \quad (2.3)$$

In this equation,  $\hbar\omega(\vec{q})$  represents the energy associated with the phonon momentum  $\vec{q}$ . To provide context pertaining to which particle we use to probe the lattice, let us consider some relevant numbers. The lattice spacing is of the order  $\sim 1.5 \text{ \AA}$  which yields a phonon wavevector of magnitude  $q = 1/(1.5 \text{ \AA}) = 10^{10} \text{ m}^{-1}$ . Keeping this in mind, we aim for an external particle capable of exchanging phonons with momentum of the order  $\vec{q} \sim 10^{10} \text{ m}^{-1}$  and the energy in meV range. . With the wavelength of the order  $5000 \text{ \AA}$  which results in a wavevector  $k_{\text{light}} = 2\pi/\lambda \approx 10^7 \text{ m}^{-1}$  of approximately  $10^7 \text{ m}^{-1}$ , light fits a possible candidate to probe the vibrational modes of lattices. However, if we look at the dispersion relation of phonon, we find that light can only probe a very small region near  $k \rightarrow 0$  around the region.

In the context of light scattering, two phenomena are commonly encountered:

- **Raman Scattering:** : This occurs when light interacts with phonons in the optical band. Optical phonons involve vibrations where atoms in the basis of the crystal lattice move out of phase with each other which often results in higher frequencies.
- **Brillouin Scattering:** Brillouin scattering, on the other hand, is observed when light interacts with acoustic phonons. Acoustic phonons involve vibrations where atoms move in phase which leads to sound wave-like propagation. .

Raman spectroscopy can provide information about both types of phonons, revealing

details about the vibrational modes of the material.

### 2.1.1 WHY RAMAN SPECTROSCOPY USUALLY EXCITES PHONONS FROM THE OPTICAL BAND

As we discussed, Raman scattering is only capable of exciting phonons for regions for which  $k \rightarrow 0$ . However for small  $k$ , acoustic photons have energy  $\nu k \ll ck$  so that energy and momentum cannot be conserved. On the other hand, optical phonons have energy  $\omega_{optical}$  which is finite for small  $k$  so that at some value of small  $k$ , we have  $\omega_{optical} = ck$  and one can match the energy and momentum of the photon to that of the phonon. Thus, whenever phonons interact with light, it is inevitably the optical phonons that are involved. However note that this does not mean that it is impossible for phonons from acoustic bands to not be excited (it's just that the probability is very low).

### 2.1.2 RAMAN-ACTIVE PHONON MODES

Raman-active phonon modes are specific vibrational modes in a crystal lattice that can interact with photons during Raman scattering. For a mode to be Raman active, it must involve a change in the polarizability  $\alpha$  of the molecule. In context of the dispersion relation of phonon shown below, we can think of it in the following manner: light waves in the crystal disperse with a constant slope of  $v = \frac{c}{n}$  where  $n$  is the refractive index. The photon and the phonon have the same frequency when the dispersion curves intersect. From the figure below, we see how this means that only modes whose frequency matches that of the laser light beam can be excited

How can we determine whether phonons will be Raman active or not? One way is through selection rules. The spectroscopic selection rule for infrared spectroscopy is that only transi-

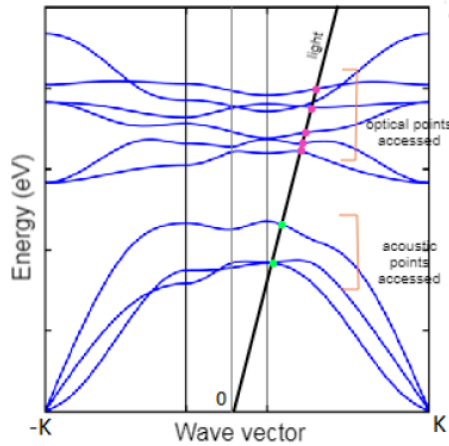


Figure 2.3: Parabolic dispersion curve graph depicting why only some modes are accessed via Raman spectroscopy

tions that cause a change in dipole moment can be observed. A general rule can be used for crystals with inversion symmetry (centrosymmetry) to examine whether modes are Raman active or IR active. In such crystals, vibrational modes can have even or odd parity (even parity modes are symmetric with respect to spatial inversion, while odd parity modes are antisymmetric). Then, only even parity modes are Raman active; this is because Raman scattering involves the interaction between the incident light and the polarizability of the molecule.

## 2.2 RAMAN SPECTROSCOPY EXPERIMENT

Let us outlay the specifications of the equipment that performs Raman Spectroscopy in our lab. To see how it works, consider the figure below:

- **532 nm Laser:** A monochromatic laser beam in the desired range is selected to excite the sample. In our case, the range is a 532 nm laser. The intensity of the laser can be adjusted by changing the power setting of the source. Note that the wavelength of the

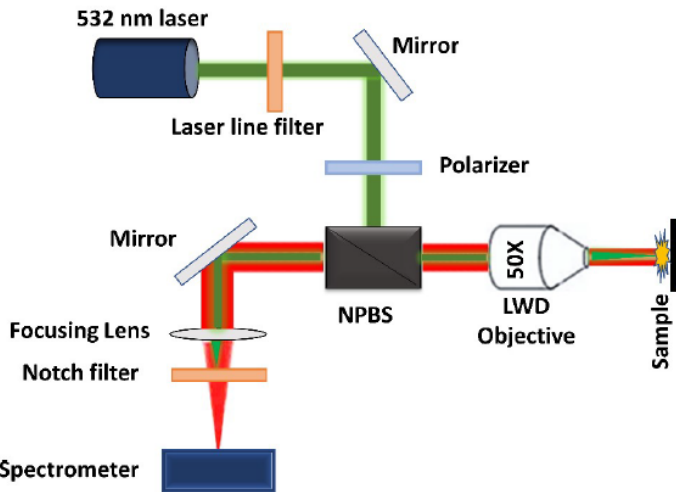


Figure 2.4: Our confocal geometry-based Raman spectroscopy lab setup

light remains fixed.

- **Laser Line Filter:** A laser line filter is used which is designed to selectively transmit a narrow range of wavelengths of light while blocking or attenuating all other wavelengths. Its primary purpose is to filter out unwanted light and allow only a specific laser wavelength to pass through.
- **Polarizer:** A polarizer is often used to control the polarization state of the laser light. It can be rotated to select a specific polarization orientation. Polarization control can provide additional information about molecular orientation in the sample.
- **NPBS:** After filtering out the light, we pass it through NPBS which is a beam splitter that splits light into two identical beams. One of the beams is directed towards the sample, while the other approaches the detector.
- **LWD objective:** The LWD objective is an objective lens with a long working distance,

meaning it can focus the laser light onto the sample from a distance without physical contact. This is particularly useful for studying samples that cannot be brought into close proximity to the lens, such as biological specimens or delicate materials.

- **Focusing Lens:** A focusing lens may be used in the collection pathway to gather the scattered Raman light from the sample. It focuses the scattered light onto the next optical component for analysis.
- **Notch Filter:** The notch filter is positioned in the Raman scattered light path after it has passed through the focusing lens. Its primary function is to block the Rayleigh scattering (unshifted laser light) and transmit only the Raman scattered light. This filter helps to enhance the signal-to-noise ratio by removing the intense laser light.
- **Spectrometer:** The spectrometer is the key instrument for Raman spectroscopy. It disperses the Raman scattered light into its constituent wavelengths (spectrum) and measures the intensity at each wavelength. The resulting Raman spectrum provides information about the vibrational modes of the molecules in the sample, allowing for chemical analysis and characterization.

### 2.3 PERFORMING RAMAN ON MoS<sub>2</sub>

Our aim when creating heterostructures is to obtain a monolayer from the bulk of MoS<sub>2</sub> that we can subsequently couple with MBI (the perovskite of our choice). This process of obtaining a monolayer from the bulk is a challenging task and in order to be sure that the sample we have extracted is indeed a monolayer (and not a bilayer or bulk), we examine the Raman plot of MoS<sub>2</sub>. Put simply, Raman spectroscopy allows us to determine if the MoS<sub>2</sub>

sample that we have obtained is indeed a monolayer or not. As to how the Raman plot give this information, that is the center of attention of our next few subsections.

### 2.3.1 IN-PLANE MODES AND OUT-OF-PLANE MODES

In-plane vibrational modes involve atomic motion within the same plane or layer of a crystal lattice. The atoms move parallel to the surface of the material. In-plane modes typically have a higher degree of symmetry because they maintain the crystal's layer-by-layer structure. Examples of in-plane modes include stretching and compressing of bonds within a single layer or shearing motions where atoms move laterally within a layer.

Out-of-Plane Modes on the other hand involve atomic motion perpendicular to the layers or planes of a crystal lattice. The atoms move in a direction that is perpendicular to the surface of the material. These modes often have lower symmetry because they can disrupt the layering of the crystal lattice. Examples of such modes involve vibrations of atoms between adjacent layers, causing the layers to move closer together or farther apart. These modes can also include changes in the spacing between layers, such as bending or buckling of the layers.

### 2.3.2 DISPERSION RELATION OF TMDCs

A crystal with  $N$  atoms per unit cell has  $3N$  vibrational modes and  $3N - 3$  optical modes. Since TMDCs have a Hexagonal Structure, a unit cell is composed of two transitional metals and four halogen atoms. As such, they have a total of 18 vibrational models. Out of these, fifteen are optical models while three are acoustic modes.

To understand the nature of these modes, let us first focus on the acoustic modes. Consider two points  $P$  and  $P_0$  on a 2D TMDC:

The atoms can vibrate along the unit vector  $\hat{n}$  which corresponds to the out of plane acous-

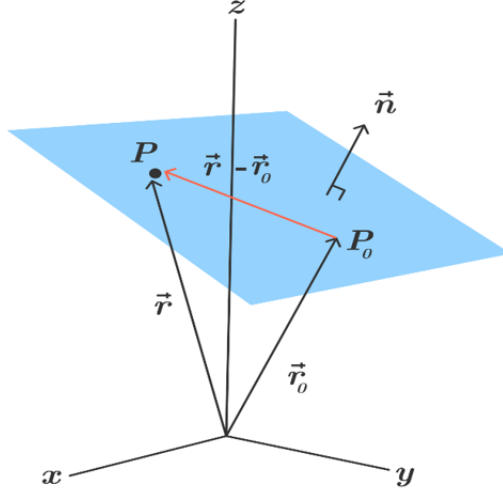


Figure 2.5: 2 points on the 2-Dimensional plane along the axis of a material

tic (ZA) mode. On the other hand, there are two in plane vibrations that are accessible to the atom of the TMDC. They can either vibrate longitudinally or in a traverse manner. We have the in-plane longitudinal (LA) and traverse acoustic (TA) mode corresponding to these vibrations respectively. The optical branches consists of two-in-plane longitudinal optical (LO<sub>1</sub> and LO<sub>2</sub>), two in-plane transverse optical (TO<sub>1</sub> and TO<sub>2</sub>) and two out of plane optical (ZO<sub>1</sub> and ZO<sub>2</sub>) modes.

The Raman spectrum of MoS<sub>2</sub> shows two primary Raman-modes, E<sub>2g</sub><sup>1</sup> and A<sub>1g</sub>. An in-plane vibration is represented by the E<sub>2g</sub><sup>1</sup> mode, whereas its out-of-plane counterpart is associated with the A<sub>1g</sub> mode. The out-of-plane vibration is influenced by its neighboring material. These two bands are first-order bands considered due to one phonon processes only.

A typical Lorentzian smoothed Raman spectrograph of MoS<sub>2</sub> showing both E<sub>2g</sub><sup>1</sup> and A<sub>1g</sub> is shown below.

As can be observed from the plot, the frequencies of the two modes E<sub>2g</sub><sup>1</sup> and A<sub>1g</sub> depend on the number of MoS<sub>2</sub> layers. The E<sub>2g</sub><sup>1</sup> peak is redshifted as the number of layers increase, while

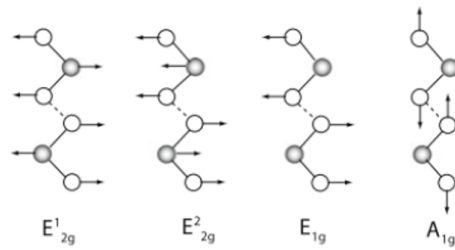


Figure 2.6: Illustration of the Raman Active Modes in the 2H polytype

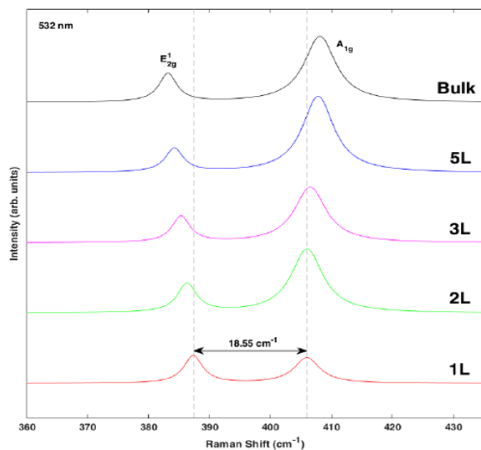


Figure 2.7: Bulk to Monolayer transition. The two vertical lines show the frequencies of the  $E_{12}^g$  and  $A_1^g$  modes for 1L.

the  $A_{1g}$  peak is blue shifted. The two peaks in the Raman spectrum correspond to softened and stiffened vibrations, respectively. The distinction in the position and intensities of these peaks has been suggested as a reliable approach for determining the thickness of the material. The separation of the two first-order modes (Raman shift) determines the number of layers. For example, the first sample, proposed to be a monolayer by optical contrast techniques, had a separation of  $18.55\text{ cm}^{-1}$ . Comparing this with literature values confirmed its identity as a monolayer. Moreover, the peak positions were also observed to be close to those obtained in the literature.

#### 2.4 PHOTOLUMINESCENCE STUDIES

Photoluminescence studies involve the measurement of light emission (photoluminescence) from a material after it has been excited by photons.

In photoluminescence studies, a material is typically excited by shining light (usually laser light) onto it. This light is absorbed by the material, exciting electrons from their lower energy states (valence band) to higher energy states (conduction band). These excited electrons leave behind "holes" in the valence band. When the excited electrons recombine with these holes, they release energy in the form of photons, which are detected as light emission. The energy (or wavelength) of the emitted light corresponds to the energy difference between the excited and relaxed states of the electrons.

For example, consider an electron in the valence band as shown in the left figure below. When a photon strikes the conductor, the electron is excited from the valence band to the conduction band (shown in the middle). This electron will then relax itself, coming back to the equilibrium state (shown in the right). In the process, it will release radiation and this process we call photoluminescence.

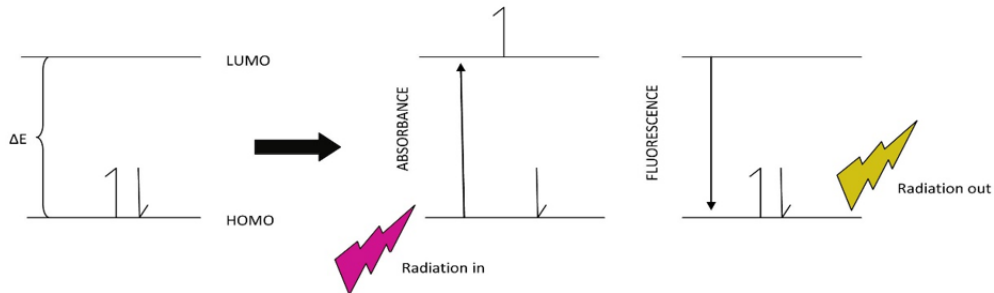


Figure 2.8: Schematic Representation of Photoluminescence Process. An electron in the valence band (left) is excited to the conduction band upon absorbing a photon (middle). The electron subsequently relaxes back to the valence band, emitting a photon in the process (right). The energy difference ( $\Delta E$ ) between the valence band (HOMO) and the conduction band (LUMO) determines the photon's energy.

## 2.5 DISTINCTION BETWEEN PHOTOLUMINESCENCE STUDIES AND RAMAN SCATTERING

In Raman Scattering, we also had an external light interacting with the material of our interest. How then does Photoluminescence studies differ from Raman Scattering? Are they the one and the same? The answer of the latter question is a definite no. The two processes are entirely distinct. To understand this, let us first consider Raman scattering. In Raman scattering, the photon undergoes an inelastic scattering which causes a shift in its momentum and energy. This change in energy corresponds to a change in its wavelength which is subsequently detected by the spectrometer. On the other hand, in photoluminescence studies, the photon is entirely absorbed. The emitted light from the sample that we observe and measure is due to the recombination of the electron-hole pairs generated by the excitation.

This explains why Raman scattering involves incident lights with lower intensity. The energy from Raman scattering is not enough to excite electrons in the valence band to the conduction band of a material. On the other hand, photoluminescence involves photons with

high enough energy to cause the electrons to transfer from the valence band to the conduction band. As a result of Photoluminescence creating an electron-hole pair, we can use PL spectroscopy to the optoelectronic properties of the material like its band gap, defect density, and charge carrier lifetime.

During PL studies, the entire photon is absorbed. However, the energy of the emitted photon by the sample is not the same as that was absorbed by photon. This is because before the electron-hole pair recombines, the electron deexcites by doing some vibrational relaxation or some internal conversion in the conduction band. Thereby, the energy of the emitted photon is reduced.

## 2.6 EXPLORING THE PL PROCESS CLOSELY

Electrons in the valence band absorb high-energy incident photons of a particular energy to jump to the conduction band, leaving a hole in the valence band. Since the electrons and holes have different thermal equilibrium distributions, they recombine radiatively and produce spontaneous emission. A PL process should then have three subprocesses:

- Excitation, in which an exciton is generated.
- Thermalization, where the charge carriers approach thermal equilibrium.
- Recombination in which the electron pair recombines after producing an emission.

During the relaxation process, an excited electron must go to the excited band's ground state. This can be done by one big direct jump or small steps towards the excited state ground state by the emission of small energy photons. Once it reaches the ground state, it recombines with its holes. This relaxation period usually is in the picosecond regime and corresponds to an excitonic emission.

By now it is clear that photoluminescence studies measure excitonic emissions. In the subsection excitons, we discussed that there are two types of excitonic emissions: free and bound. To understand the distinction between the PL spectra of these two, we must consider closely their stability. Recall that binding energy represents the energy required to dissociate an exciton into its constituent electron and hole charge carriers.

- **Free Excitons:** Free exciton has small binding energies ( $\sim 0.01$  eV) therefore it is very easy to dissociate them into their constituent electron and hole. As such, they are unstable at room temperature ( $k_B T \sim 0.025$  eV).
- **Bound Excitons:** Bound excitons have binding energy around  $0.1 - 1$  eV which is why they are stable at room temperature.

Because the binding energy of Bound excitons is large, their exciton PL is strong even at room temperature.

## 2.7 EQUIPMENT AND SETUP

The equipment for PL spectroscopy is the same as that of Raman Spectroscopy. Both PL and Raman spectroscopies typically require a monochromatic light source, such as a laser, focused onto the sample. The scattered light is then collected and analyzed using a spectrometer. However, the type of spectrometer used differs for the two techniques. For Raman spectroscopy, a spectrometer equipped with a narrow-bandwidth filter is commonly used. This is because the challenge in Raman Spectroscopy is that the Raman Scattered light is usually very weak compared to the intense laser excitation. A narrow-bandwidth filter allows only a very narrow range of wavelengths, centered around the Raman-shifted wavelength to pass through. On the other for PL spectroscopy, a spectrometer fitted with a long-pass or band-pass filter is

used. This is because in PL spectroscopy, the challenge is to isolate the photoluminescence signal from the excitation laser light. The long-pass filter successfully allows the photoluminescence light to pass through since it has less energy and therefore higher wavelength. However, it blocks the excitation light which has high energy and a lower wavelength.

Additionally, low-temperature PL spectroscopy requires a cryostat to maintain the sample at a low temperature and avoid thermal effects on the photoluminescence signal. In contrast, Raman spectroscopy can be performed at room temperature, although it may also benefit from cooling to reduce thermal effects.

## 2.8 PHOTOLUMINESCENCE CHARACTERISTICS OF MoS<sub>2</sub>

As stated before, in PL Spectroscopy we monitor the radiative recombination of electrons back to the valence band. During photoluminescence, MoS<sub>2</sub> layers absorb photons, which leads to the formation of excitons. In MoS<sub>2</sub>, excitons can exist in two different states: the A exciton and the B exciton. They can exist in two states only due to the direct band gap structure of MoS<sub>2</sub>. As was previously discussed, the K and K' valleys in the Brillouin zone are degenerate, which allows for the formation of excitons in either valley.

## 2.9 PHOTOLUMINESCENCE SPECTROSCOPY OF MoS<sub>2</sub>

The PL spectrum of MoS<sub>2</sub> monolayer and bilayer is shown in the figure below.

In the monolayer, the A exciton is detected at  $\sim 1.85$  eV, originating from the emission of negative trions excitons ( $X^-$ ). On the other hand, the B exciton is observed at  $\sim 2.01$  eV, which results from the emission of neutral excitons ( $X$ ). In the bilayer, the A exciton's energy is  $\sim 1.84$  eV, which is slightly lower than that of its monolayer counterpart. These results match well with those calculated in the literature. The excitation energy is observed at 2.33 eV

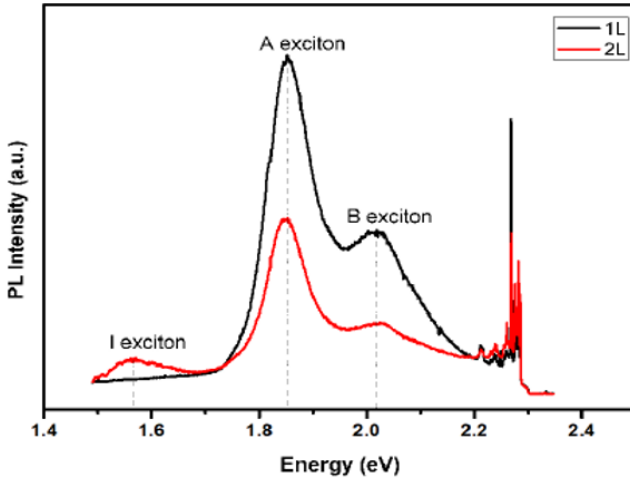


Figure 2.9: The PL spectra of A and B Excitons for MoS<sub>2</sub> monolayer and bilayer

due to the use of 532 nm laser is used. Si and MoS<sub>2</sub> peaks are also observed between 2.2 and 2.3 eV.

As the number of layers increases, the energy required to create an exciton decreases, as evidenced by the redshift in the excitonic emission energy as the number of layers increase. This is because of the increased screening of the Coulomb interaction between the electron and hole by neighboring layers. This also implies that the exciton binding energy decreases as the number of layers increases; it can be calculated from the energy difference between the excitonic absorption and emission peaks. Lower energies are emitted when excitons recombine, so the energy required to create an exciton decreases with increasing layers.

Additionally, the A and B exciton energies split as the number of layers increases, with the A exciton energy decreasing and the B exciton energy increasing. This splitting is due to the influence of the interlayer coupling between adjacent layers. With increasing layers, the coupling increases, resulting in a more significant splitting between the energies of the two excitons. This is because the A exciton is strongly localized within a single layer, while the B

exciton is spread over several layers. Therefore, the interlayer coupling affects the B exciton more than the A exciton, resulting in a larger splitting between the two excitonic energies.

The photoluminescence intensity is also observed to decrease as the number of layers goes from the monolayer to the bilayer, as the excitons in the monolayer are more strongly bound and have longer lifetimes, leading to fewer recombination events. The indirect band gap of the increasing number of MoS<sub>2</sub> layers causes the PL to get weaker. An extra peak, I, observed at  $\sim 1.56\text{eV}$  in the bilayer, indicates the band gap shift to an indirect one. The A and B excitons remain comparable to their monolayer counterparts. The indirect exciton at  $1.56\text{ eV}$  in the bilayer and higher layers is significant for layer number identification since the positions of the A and B excitons remain the same. It is important to note that the theoretical band gaps reported for layers beyond the monolayer rely on the position of the indirect exciton.

## 2.10 TEMPERATURE DEPENDENT PHOTOLUMINESCENCE SPECTROSCOPY OF MBI

Since MBI has emerged relatively recently, there are few studies which comprehensive analysis of its photoluminescence properties. Consequently, we performed temperature-dependent PL spectra of MBI and compare it with the properties of other extensively studied perovskites. Our studies indicate that MBI displays a photoluminescence spectrum with multiple components consisting of free excitons, self-trapped excitons, and donor-acceptor pair recombination. At low temperatures, the PL spectra show more complex peak behavior, while at higher temperatures, defects and excitonic traps significantly influence the emission. These defect states can arise from various sources such as crystal lattice distortions, atomic ionization, and systematic assembly defects in the perovskite structure. Additionally, the movement of the organic cation in the perovskite can lead to the formation of self-trapped excitons.

The PL spectra were obtained through temperature-dependent measurements ranging

from 88 K to 295 K on bulk MBI (spin-coated on a mesoporous layer) in a cryogenic chamber at  $50 \mu\text{W}$  power. Measurements were taken at each temperature for 20-30 seconds using a 405 nm laser for optical excitation and a 675 nm diode laser. Repeated measurements accounted for temperature fluctuations, and the results were normalized and averaged. Additionally, the room temperature UV-Vis spectrum of MBI was plotted (see the figure below).

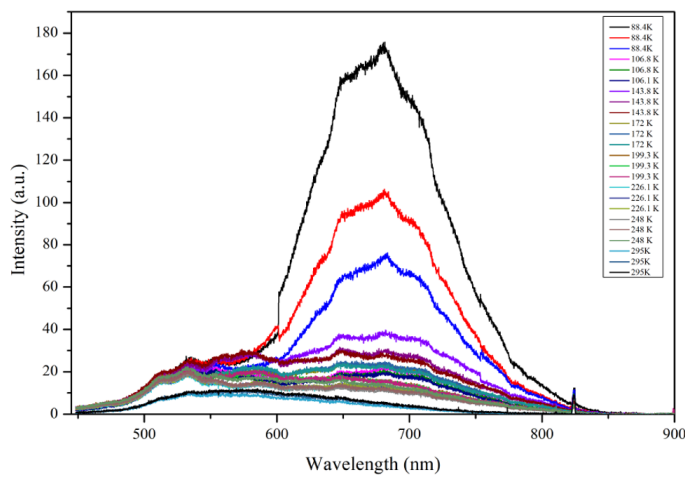


Figure 2.10: Temperature Dependent MBI in the temperature range 88.4-295 K.

The UV-Vis absorption spectrum of a perovskite shows the material's light absorption at different wavelengths, providing information about the band gap, electronic structure, and any defects or impurities. The onset of absorption in the UV region estimates the band gap energy while the spectrum's shape and intensity reveal details about excitonic transitions and charge carrier dynamics. For MBI, extrapolating the steepest linear increase of light absorption to the x-axis yields an estimated band gap of  $\sim 2.15$  eV. This guides the selection of an excitation laser for further experiments.

From the temperature-dependent PL spectra in the figure above, a general trend is observed: as temperature increases, PL intensity decreases, and the dominant peak redshifts and

narrows at lower temperatures. The emission may correspond to band-to-band charge recombination with the band gap changing from  $\sim$  2.1 eV at room temperature to  $\sim$  1.84 eV at 88.4 K. Factors such as defect density, carrier concentration, and charge transport properties influence the efficiency of this recombination process. This efficiency can be reduced by defects or impurities acting as recombination centers and trapping charge carriers.

In general, MBI's PL spectrum shows similarities to that of methylammonium lead iodide (MLI), where structural phase transitions influence PL behavior. Studies suggest that the peak shift towards higher energies in MLI can be attributed to the thermal activation of trapped excitons. These excitons, confined to specific regions due to defects or impurities, require higher energy to be freed. The thermal activation energy can be estimated by fitting peak energy values versus temperature to an Arrhenius plot. In MBI, additional peaks may appear in the PL spectra depending on temperature and excitation intensity, broadening and decreasing in intensity with increased temperature due to exciton dissociation and defect state formation.

Deconvolution of single-temperature peaks, a technique used for MLI, can also be applied to MBI to identify contributions from free excitons and defects. Without deconvolution, similarities between MBI and MLI are evident, particularly in temperature-dependent PL spectra. The Gaussian deconvolution of MLI's PL spectrum at specific temperatures shows four distinct peaks, corresponding to energy values of 1.65 eV, 1.6 eV, and 1.48 eV for MLI, and approximately 2.23 eV, 2.33 eV, and 2.42 eV for MBI, after converting wavelengths to energy (see figure below).

One notable difference is the improbability of phase transitions in methylammonium bis-muth iodide compared to other perovskites. Studies on bismuth-based perovskites, such as  $(CH_3NH)_4Bi_6I_{22}$ , show no phase transitions but rather attribute PL behavior to irregular unit cell contractions at low temperatures, impacting the band gap. They also link the slow

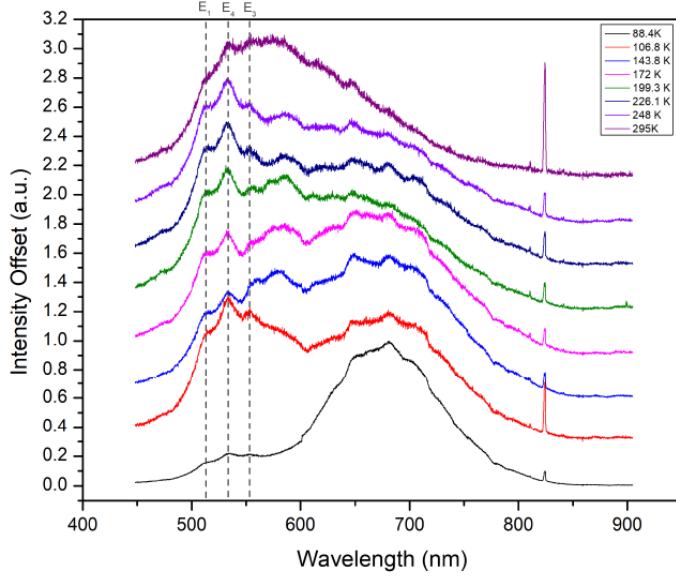


Figure 2.11: Deconvolved MBI PL Spectra. Intensity offset plotted for the temperature-dependent PL spectra of MBI.

redshift in emission peak with increasing temperature due to the thermal expansion of the crystal lattice, which decreases the band gap energy. This observation contrasts with the behavior of MBI, suggesting a need for further investigation into MBI's phase transitions and heat capacity curves to understand its PL behavior comprehensively.

# 3

## Synthesis in Lab

This subsection explores the experimental procedures carried out towards the aim of creating the heterojunction in our laboratory. The following are the two subprocesses that we carried out towards these aims:

- The mechanical exfoliation of MoS<sub>2</sub> bulk and its subsequent transfer onto the silicon.

This sample is examined under an optical microscope to look for a monolayer. If a

promising sample is identified, further spectroscopic studies are conducted on it to corroborate and confirm the existence of a monolayer.

- Various transfer methods are utilized to transfer MoS<sub>2</sub> monolayer onto a MBI perovskite sample on Silicon. A successful transfer will result in the fabrication of MoS<sub>2</sub>-MBI heterojunction that we desire, on which we will perform further Raman and PL spectra studies.

### 3.1 CLEANING SILICON WAFER

When preparing the sample that we subsequently look under the microscope, we initially begin with a silicon sample. We cut this sample into approximately 10 × 10 mm squares using a diamond cutter to obtain silicon wafers. These silicon wafers are subsequently cleaned with the cleaning method involving the following procedures:

- Silicon is submerged in a plastic bottle that contains deionized (DI) water and soap and is then sonicated for 15-20 minutes.
- Rinse the sample from the previous step with DI water after removing it from the bottle. Sonicate the silicon submerged in DI water only for 15 minutes.
- Sonicate the substrate in isopropyl alcohol (IPA) for 15 minutes. This will make the substrate surface hydrophobic.
- Sonicate the substrate in acetone for 15 minutes.
- Sonicate the substrate in IPA again for 15 minutes.
- Finally, sonicate the substrate in DI water for 15 minutes.

- Dry the samples with nitrogen.
- Place the samples on a hot plate (with the shiny side of silicon up) for 10 minutes.

After this process, a clean lint-free tissue is used to wipe off any water marks.

### 3.2 DRY TRANSFER OF 2D MATERIALS USING PDMS LAYER

Viscoelastic materials such as Polydimethylsiloxane (PDMS) exhibit both viscous (flowing) and elastic (spring-like) properties. When subjected to stress, these materials can deform and subsequently return to their original shape once the stress is removed. However, they also exhibit some degree of flow or deformation over time. Consequently, PDMS films behave as an elastic solid on short-term scales but as a viscous fluid on longer-term scales. This gives them a kinematically controlled adhesion property where the speed at which an object is pulled off from the film's surface directly influences the strength of the adhesion force it experiences. As such, PDMS-based transfer methods provide a rapid and convenient means of depositing 2D materials onto nearly any substrate without the need for wet chemistry. In order to remove a substrate from the PDMS, we slowly peel off the substrate from the PDMS (so that it experiences less adhesion force). However, in order to stick the substrate onto the PDMS, we quickly peel off the substrate onto the PDMS (causing it to experience high adhesion force).

Creating PDMS in the lab is a relatively easy process requiring an hour or two. Firstly, we prepare the elastomer mix. This involves the following steps:

1. Turn the digital scale on, placing the plastic weighing dish on it and taring.
2. Pour 28g of elastomer base onto the weighing dish followed by 4g of elastomer curing agent.

3. Mix the base and curing agent together for 10 minutes using a stirring tool. Use a pipette tip to burst the largest bubbles in the mixture.
4. To burst the remaining bubbles, place the plastic dish inside your desiccator and desiccate for 5 minutes. After 5 minutes, open and close the valve suddenly - this will pop the bubbles left in the mixture.
5. Repeat this process at least three times until all bubbles have burst.
6. Release pressure in your desiccator and remove the weighing tray.

We then transfer the elastomer mix onto a glass plate which involves the following steps:

1. Place the plate on a baking tray and ensure it is resting in a flat position to ensure the PDMS spreads out uniformly thick.
2. Pour the elastomer mix onto the center of the glass plate leaving a border along the edges of the plate.
3. If any bubbles form while pouring, use a pipette tip to burst them.
4. Dispose of your weighing dish with the remaining PDMS mixture.
5. Leave the mix to sit for one hour, in this time the elastomer mix should spread evenly across the glass plate.

Finally, we cook the sample and cut to size, involving the following processes:

1. Once the oven has come to temperature, place the baking tray with the glass plate on it inside.
2. Set a timer and cook the PDMS for one hour.

3. After one hour, take the PDMS out of the oven and leave to cool for at least 45 minutes, or until cool to the touch.
4. Using a ruler and exacto knife cut off the indoor mounting tape from the edges of the PDMS. Peel the PDMS off the glass plate carefully, avoiding tears.
5. Place your piece of PDMS on a cutting board. Place a chip of the desired dimensions on the PDMS avoiding areas with bubbles or embedded debris. Using the exacto knife, cut around the perimeter of your chip.

When transferring MoS<sub>2</sub> crystals onto the PDMS from bulk, we use a PDMS sample of approximately 3 mm thickness and 1 cm length. This sample is attached to a glass slide using double tape.

### 3.3 MECHANICAL EXFOLIATION



Figure 3.1: Mechanical Exfoliation. Thinner layers are obtained by progressively pressing the tape to itself and unpeeling it.

With our PDMS sample prepared and our silicon wafers cleaned, we are ready to move

to the next procedure involving our experiment which is the mechanical exfoliation of bulk MoS<sub>2</sub> onto the PDMS attached to the glass slide and subsequently silicon wafer.

Mechanical exfoliation is a technique used to obtain thin flakes or layers of 2D materials, such as graphene or transition metal dichalcogenides (TMDCs), from a bulk sample by cleaving or peeling. In our laboratory, we primarily employ the scotch tape method, a common approach for mechanical exfoliation. This method involves placing a small sample of the bulk material on a piece of tape and then peeling it off by pressing the tape onto itself. Through multiple repetitions, this process progressively yields thinner layers, as illustrated in the accompanying figure.

In TMDCs, the interlayer bonding is weaker compared to the material's van der Waals attraction to the substrate. However, there's a challenge in transferring extremely thin crystal layers to a substrate—while thinner layers adhere well to the tape, making the transfer more difficult. It's noteworthy that this method does not transfer the entire crystal onto the tape. To optimize results, it's advisable to press the tape against itself only once or twice, as repetitive peeling may reduce the lateral dimensions of the layers.

After this, the tape containing these crystals is pressed onto the PDMS attached to a glass slide and left on it for about a minute to ensure adhesion. It is then swiftly pulled off from the PDMS, where recall that faster pull off rates cause substrate to stick to the PDMS. We then gently press the PDMS slide containing MoS<sub>2</sub> crystals onto the silicon wafer and subsequently examine the sample under an optical microscope for a monolayer. This method of mechanical exfoliation does not guarantee success in a single attempt, and several repetitions may be necessary before a monolayer is found.

### 3.4 LOOKING FOR A MONOLAYER UNDER A MICROSCOPE

After we have taken silicon layer with MoS<sub>2</sub> on it in the dry lab, we observe the sample under a microscope to look for a monolayer. This involves looking at a sample under (50x) magnification. The figure below shows what a typical sample appears like:

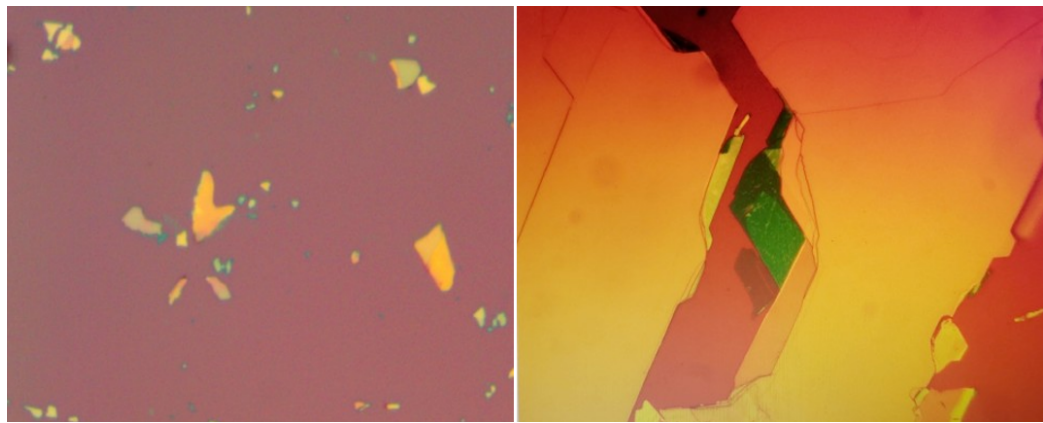


Figure 3.2: MoS<sub>2</sub> flakes at x10 at x50 respectively. Often, monolayer and bilayers are found attached at the edge of bulk material

We observe the following along with their identification:

- Orange is the background color.
- Yellow objects under the microscope are the bulk material.
- The green objects are polylayers, which are less in spatial extent than bulk material.
- The pale layers, which appear almost as shadows to the background color (for example, the one next to the green layer), are bilayers.
- The even paler layer is the monolayer.

Usually, there is only a single monolayer per sample, and therefore the task of searching for the monolayer takes a thorough examination of the entire sample. Note that it is important that the monolayer is not very thin, or else we would not be able to use it meaningfully to create a heterostructure. As such, when looking under a magnification of  $\times 50$ , the monolayer should occupy at least a sizable part of the view in order for a successful spectrum to be obtained on it.

For samples containing potential monolayers, we perform Raman Spectroscopy, the details of which we have already discussed in detail above. If the distance between the in-plane vibrational mode  $E_{2g}^1$  and out-of-plane vibrational mode  $A_{1g}$  is approximately in the range  $18.55\text{ cm}^{-1} - 18.70\text{ cm}^{-1}$ , we have a monolayer. Otherwise, for distances bigger than those, we are dealing with polylayers.

### 3.5 SYNTHESIS OF HETEROJUNCTION

The creation of heterostructure in our lab was divided into three parts. First, we needed to frequently reproduce a  $\text{MoS}_2$  monolayer to improve repeated methods. Second, we had to successfully deposit perovskite samples on a substrate. Finally, we needed to devise a suitable method for establishing contact between the two materials.

Initially, our group combined mechanical exfoliation and PDMS transfer methods to produce thin layers of  $\text{MoS}_2$ .  $\text{MoS}_2$  was mechanically exfoliated and transferred onto PDMS, then to silicon. Our group tried transferring perovskite crystals onto silicon using a mesoporous titania layer. The goal was to have perovskite deposits on silicon, onto which a  $\text{MoS}_2$  monolayer could be transferred from PDMS. However, the combination of methods did not yield promising results.

Three methods of transferring MBI onto silicon were explored:

1. Using PDMS and tape (**Figure a**): MBI was picked up using PDMS and moved to silicon with tape.
2. Direct contact (**Figure b**): A silicon wafer was placed upside down on the perovskite deposit and gently slid over the crystal.
3. PDMS stamp transfer (**Figure c**): This method proved better, transferring more concentrated MBI onto silicon.

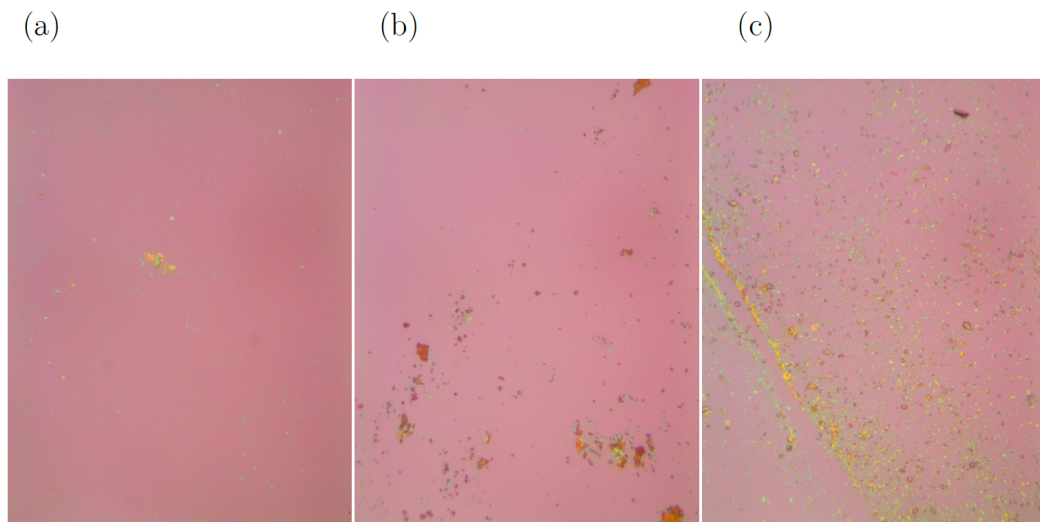


Figure 3.3: MBI deposits on silicon at a magnification of 50x. (a) Mechanical exfoliation of MBI. (b) Deposits via direct contact between silicon and MBI. (c) Deposits by the PDMS transfer method

We observed the amount of MBI on the sample and compared it with the amount transferred by PDMS onto silicon. Our findings showed that PDMS transferred a considerable amount of MBI onto silicon, but the samples were not large enough for PL measurements. We transferred MBI onto silicon with MoS<sub>2</sub> deposits, confirming that concentrated samples were insufficient for further analysis.

Our findings indicated the problem was the size of deposited flakes. To obtain larger flakes, we spin-coated perovskite samples on silicon to achieve a uniform layer of crystals with hexagonal deposits up to 0.02 mm in size. Overlapping regions offered deposits up to 0.08–0.1 mm. We aimed to deposit MBI on this setup while controlling the number of layers transferred onto the perovskite crystal.

Mechanically exfoliated MoS<sub>2</sub> crystals were transferred onto PDMS and identified using optical microscopy. The PDMS was supported on a glass slide using double-sided tape, then adjusted on the upper stage. The spin-coated MBI on silicon was placed on the lower stage, and both stages were brought close until fringes appeared, indicating contact. However, under an optical microscope, no material transfer was observed. We adjusted the alignment but achieved the same result, leading us to conclude that spin-coated MBI does not stick to MoS<sub>2</sub> due to their smooth surfaces and lack of interaction.

### 3.5.1 HAND STAMPING METHOD

Motivated by these observations, we tested if deposition occurs with greater force. We hand-pressed MoS<sub>2</sub> on PDMS against MBI on silicon using lab forceps, sliding the samples to increase friction and promote deposition. We investigated the samples to check for material transfer. Figure a) shows MBI deposited on MoS<sub>2</sub> on PDMS, while Figure b) shows minimal MoS<sub>2</sub> deposits on silicon with spin-coated perovskite.

This method proved promising, as sizable MBI pieces were found on MoS<sub>2</sub> layers. Different thicknesses of perovskite layers were deposited, with outlines of some MoS<sub>2</sub> bulk crystals visible underneath the MBI crystals. Since this was only a preliminary test, this method was selected for further investigation for optoelectronic measurements on the heterostructure. We also tested a derivative method, switching the materials on both substrates. MoS<sub>2</sub> flakes on

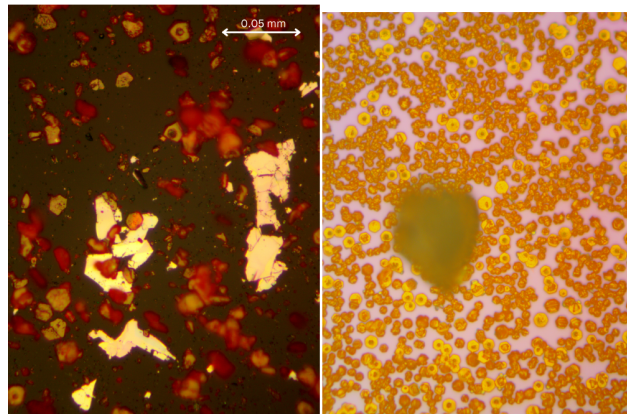


Figure 3.4: Optical Images at 50x magnification. Figure on the left: MBI deposits on MoS<sub>2</sub> crystals on PDMS. Figure on the right: MoS<sub>2</sub> deposit on Si spin coated with MBI.

silicon were pressed against MBI on PDMS, but this method had the same issue as previous transfer methods, with minimal MBI deposits on MoS<sub>2</sub>.

# 4

## Conclusion

The core objective of this research was to fabricate a functional MoS<sub>2</sub>/MBI heterostructure and to investigate its optoelectronic properties. The following were the key findings of our study thus far,

- **Mechanical Exfoliation and Monolayer identification:** The mechanical exfoliation process using the Scotch tape method proved effective in isolating monolayers of

$\text{MoS}_2$ . The identification of these monolayers was confirmed using optical microscopy and Raman spectroscopy. The Raman spectra provided distinct signatures that allowed us to differentiate between monolayers and multilayers, ensuring the accuracy of our sample preparation. However, the Scotch tape method suffers from inconsistent yields of monolayer which is far from ideal for our attempts for creating heterojunctions on a consistent basis. As such, our study would be greatly advanced if more consistent methods of isolating monolayers from bulk  $\text{MoS}_2$  are explored.

- **Transfer Methods and Heterojunction formation:** Various transfer methods, including PDMS-based transfer and direct contact methods, were employed to deposit  $\text{MoS}_2$  monolayers onto MBI-coated silicon substrates. The main problem that we faced was that the spin-coated MBI does not stick easily to  $\text{MoS}_2$ . While the hand stamping method showed promise in achieving more consistent material transfer, it represents only one of the many possible solutions to the problem. This leaves space for further refinement and optimization of the study.
- **Spectroscopic Characterization:** Raman spectroscopy and photoluminescence (PL) studies were instrumental in characterizing the materials. The Raman spectra of  $\text{MoS}_2$  provided insights into the vibrational modes and confirmed the presence of monolayers. PL studies revealed the excitonic properties of both  $\text{MoS}_2$  and MBI, highlighting their complementary absorption characteristics. The temperature-dependent PL spectra of MBI indicated the presence of multiple emission components, influenced by defects and excitonic traps, which are crucial for understanding its optoelectronic behavior.

The successful fabrication of Heterojunction can potentially pave the way for further

fruitful studies. These include but are not limited to estimating open-circuit voltage ( $V_{oc}$ ), short-circuit current ( $I_{sc}$ ), Fill Factor (FF) and Power Conversion Efficiency (PCE) of our synthesized heterostructures. Further experiments can be carried out to delve deeper into the dynamics of charge carriers which included their lifetimes and diffusion lengths. Time-resolved photoluminescence and transient absorption spectroscopy can be employed to study these properties in  $\text{MoS}_2$ /MBI heterostructures. Furthermore, investigating the stability of  $\text{MoS}_2$ /MBI heterostructures under various environmental conditions such as temperature, humidity, and light exposure will be essential for accessing their practical application in solar cells. In conclusion, continued exploration and a dedicated attempt for the synthesis of this heterostructure can pave the way for innovative solutions in optoelectronics, particularly in the development of high-efficiency, stable, and scalable solar cells.

# References

- [1] Bai, F., Qi, J., Li, F., Fang, Y., Han, W., Wu, H., & Zhang, Y. (2018). A high-performance self-powered photodetector based on monolayer mos<sub>2</sub>/perovskite heterostructures. *Advanced Materials Interfaces*, 5(6), 1701275.
- [2] Chernikov, A., Berkelbach, T. C., Hill, H. M., Rigos, A., Li, Y., Aslan, B., Reichman, D. R., Hybertsen, M. S., & Heinz, T. F. (2014). Exciton binding energy and nonhydrogenic rydberg series in monolayer ws<sub>2</sub>. *Phys. Rev. Lett.*, 113, 076802.
- [3] Demtröder, W. (1973). *Laser spectroscopy*, volume 2. Springer.
- [4] Griffiths, D. J. (2023). *Introduction to electrodynamics*. Cambridge University Press.
- [5] Jiang, Y., Chen, S., Zheng, W., Zheng, B., & Pan, A. (2021). Interlayer exciton formation, relaxation, and transport in tmd van der waals heterostructures. *Light: Science & Applications*, 10(1), 72.
- [6] Keldysh, L. (2024). Coulomb interaction in thin semiconductor and semimetal films. In *SELECTED PAPERS OF LEONID V KELDYSH* (pp. 155–158). World Scientific.
- [7] Kittel, C. & McEuen, P. (2018). *Introduction to solid state physics*. John Wiley & Sons.
- [8] Landau, L. D. & Lifshitz, E. M. (2013). *Quantum mechanics: non-relativistic theory*, volume 3. Elsevier.
- [9] Pelant, I. & Valenta, J. (2012). *Luminescence spectroscopy of semiconductors*. OUP Oxford.
- [10] Piper, J. R. & Fan, S. (2016). Broadband absorption enhancement in solar cells with an atomically thin active layer. *Acs Photonics*, 3(4), 571–577.
- [11] Rytova, N. S. (2018). Screened potential of a point charge in a thin film. *arXiv preprint arXiv:1806.00976*.
- [12] Simon, S. H. (2013). *The Oxford solid state basics*. OUP Oxford.

- [13] Van der Donck, M. & Peeters, F. (2018). Interlayer excitons in transition metal dichalcogenide heterostructures. *Physical Review B*, 98(11), 115104.
- [14] Yang, X., Guo, S., Chan, F., Wong, K., & Ching, W. (1991). Analytic solution of a two-dimensional hydrogen atom. i. nonrelativistic theory. *Physical Review A*, 43(3), 1186.
- [15] Zou, X., Xu, Y., & Duan, W. (2021). 2d materials: rising star for future applications. *The Innovation*, 2(2).

**T**HIS THESIS WAS TYPESET using L<sup>A</sup>T<sub>E</sub>X, originally developed by Leslie Lamport and based on Donald Knuth’s T<sub>E</sub>X. The body text is set in 11 point Egenolff-Berner Garamond, a revival of Claude Garamont’s humanist typeface. The above illustration, “Science Experiment 02”, was created by Ben Schlitter and released under CC BY-NC-ND 3.0. A template that can be used to format a PhD thesis with this look and feel has been released under the permissive MIT (x11) license, and can be found online at [github.com/suchow/Dissertate](https://github.com/suchow/Dissertate) or from its author, Jordan Suchow, at [suchow@post.harvard.edu](mailto:suchow@post.harvard.edu).